Manuscript 7325 revision 1

Quadrivalent praseodymium in planetary materials

Michael Anenburg[1,*], Antony D. Burnham[1] and Jessica L. Hamilton[2]

[1]Research School of Earth Sciences, Australian National University, Canberra ACT 2600, Australia

[2]Australian Synchrotron, ANSTO, Clayton, VIC 3168, Australia

[*]email: michael.anenburg@anu.edu.au

Abstract

Praseodymium is capable of existing as Pr^{3+} and Pr^{4+}. Although the former is dominant across almost all geological conditions, the observation of Pr^{4+} by XANES and Pr anomalies (both positive and negative) in multiple light rare earth element minerals from Nolans Bore, Australia and Stetind, Norway, indicates that quadrivalent Pr can occur under oxidizing hydrothermal and supergene conditions. High-temperature REE partitioning experiments at oxygen fugacities up to more than 12 log units more oxidizing than the fayalite-magnetite-quartz buffer show negligible evidence for Pr^{4+} in zircon, indicating that Pr likely remains as Pr^{3+} under all magmatic conditions. Synthetic Pr^{4+}-bearing zircons in the pigment industry form under unique conditions which are not attained in natural systems. Quadrivalent Pr in solutions has an extremely short lifetime, but may be sufficient to cause anomalous Pr in solids. Because the same conditions that favors Pr^{4+} also stabilize Ce^{4+} to a greater extent, these two cations have similar ionic radii, and Ce is more than six times as abundant as Pr, it seems that Pr-dominant minerals must be exceptionally rare, if they occur at all. We identify cold, alkaline, and oxidizing environments such as oxyhalide-rich regions at the Atacama Desert or on Mars as candidates for the existence of Pr-dominant minerals.

This is the peer-reviewed, final accepted version for American Mineralogist, published by the Mineralogical Society of America.
The published version is subject to change. Cite as Authors (Year) Title. American Mineralogist, in press.
DOI: https://doi.org/10.2138/am-2020-7325. http://www.minsocam.org/

Introduction

The lanthanides (La to Lu) and yttrium are known as the rare earth elements (REE), a group which exhibits strikingly similar geochemical properties, stemming from their electronic structure. They form trivalent cations whose radius decreases with increasing Z because of weak shielding of the other electrons by the 4f shell (e.g. $_{58}Ce^{3+}$ = [Xe]$4f^1$, $_{59}Pr^{3+}$ = [Xe]$4f^2$, …, $_{71}Lu^{3+}$ = [Xe]$4f^{14}$). For example, the diameter of La^{3+} is 116 pm whereas that of Lu^{3+} is 97.7 pm (Fig. 1), a phenomenon known as the lanthanide contraction. The combination of identical ionic charge and smoothly varying radius makes the geochemistry of the REE mostly simple and predictable. However, under oxidizing conditions, Ce loses four electrons instead of three resulting in a closed shell ($_{58}Ce^{4+}$ = [Xe]$4f^0$).

Although the crustal abundance of Ce is only ~60 ppm (Rudnick and Gao, 2014), fractionating processes can concentrate it to the point where Ce-dominant minerals crystallize. Indeed, there are more than 150 known minerals with essential Ce in their formulas. The majority of these minerals contain Ce^{3+} as expected and their names contain the "-(Ce)" Levinson suffix when Ce dominates relative to the other REE (e.g. monazite-(Ce)–$Ce^{3+}PO_4$, fluocerite-(Ce)–$Ce^{3+}F_3$, or bastnäsite-(Ce)–$Ce^{3+}CO_3F$, when considering their ideal chemical formulas), but there are three known exceptions: stetindite-(Ce) ($Ce^{4+}SiO_4$), cerianite-(Ce) ($Ce^{4+}O_2$), and dyrnaesite-(La) ($Na_8Ce^{4+}(La,REE)_2(PO_4)_6$). Other minerals such as zircon and baddeleyite similarly exhibit a strong preference for Ce^{4+} over Ce^{3+}, resulting in a deviation of REE patterns from the aforementioned smooth behavior expected for purely trivalent REE (Burnham and Berry, 2012, 2014). Accurate modelling of REE in geological systems requires knowledge of the likely REE anomalies arising from redox variability. Therefore, it is important to establish whether, and to what extent, other REE change their oxidation states. Europium is the best known, occurring as Eu^{2+} under reducing conditions (Burnham et al., 2015), with Ingrao et al. (2019) showing that Sm and Yb can also be

49 divalent under ultra-reducing conditions such as those observed in some extraterrestrial
50 materials.

51 After Ce, the most likely candidate to undergo oxidative redox changes is Pr. On Earth's
52 surface, pure Pr oxide is stable as commercially available mixed-valence oxide: Pr_6O_{11}:
53 $4Pr^{4+}O_2 \cdot Pr_2^{3+}O_3$ (Martin, 1974; Suzuki et al., 2009). Pure quadrivalent Pr is not known so far
54 from natural materials and is uncommon in synthetic materials (Willauer et al., 2020). This
55 raises the question of whether Pr^{4+} exists in nature, to what degree, and can any anomalous
56 behavior stemming from the higher oxidation state be detected or predicted.

57 In this study we examine the known Ce^{4+}-bearing minerals, which are obvious candidates for
58 inclusion of other quadrivalent REE. We assess whether their chemical composition shows
59 evidence for the presence of Pr^{4+}. We show experimental evidence from zircon, a common
60 mineral which demonstrates Ce anomalies. We then discuss the possibility of Pr^{4+} occurring
61 in nature and compare them to REE^{3+} minerals in the context of mineral evolution (Hazen
62 and Ausubel, 2016; Hazen et al., 2015).

63 **Methods**

64 We conducted two zircon synthesis experiments. The P-free starting mix used in the
65 experiments of Burnham and Berry (2012) was decarbonated at 1000 °C. The resulting
66 powder was loaded into two capsules to achieve oxidizing and reducing conditions. In the
67 "oxidized" experiment the mix was placed in a 3.5 mm diameter Pt capsule between two
68 layers of PtO_2. In the "reduced" experiment the mix was placed inside a graphite capsule (2.5
69 mm inner diameter) within a 5 mm diameter Pt capsule. The capsules were crimped, welded
70 and placed at the center of ½" MgO–graphite–Pyrex–NaCl assemblies in an end-loaded
71 piston cylinder apparatus. The pressure was raised to 1.0 GPa and the temperature was
72 monitored by Type-B thermocouple and was raised at 6 °C/min to 1380 °C and held for 4

hours, cooled at 2 °C/hr to 1300 °C and held for 1 hour prior to quenching to room temperature by cutting the power to the heater. The capsules were recovered, and the contents exposed for analysis by grinding and polishing with SiC and diamond powders. Specimens of REE-rich minerals from Stetind (Norway) and Nolans Bore (Australia) were mounted in epoxy and prepared in the same way as the experimental samples.

REE patterns were calculated from REE concentrations acquired using LA-ICP-MS. We used a 193 nm ArF excimer (Coherent CompexPro 110) laser ablation system, and an Agilent 7700 quadrupole ICP-MS with dual-mode discrete dynode electron multiplier detector. The ablation was conducted in a custom-built "HelEx" two-volume vortex sampling cell in an atmosphere of He and Ar. Material was ablated at a frequency of 5 Hz and transported to the ICP-MS in this gas mixture, with a small amount of H_2 added during sample introduction for interference minimization. The laser energy was 80 mJ, with an operating fluence at the sample surface of ~9.25 J/cm^2, and a spot size of 28 µm. The following isotopes are reported in this study: ^{29}Si, ^{43}Ca, ^{139}La, ^{140}Ce, ^{141}Pr, ^{146}Nd, ^{147}Sm, ^{153}Eu, $^{155, 156, 157}$Gd, ^{159}Tb, ^{163}Dy, ^{165}Ho, $^{166, 167}$Er, ^{169}Tm, ^{172}Yb, ^{175}Lu. Multiple isotopes of Gd and Er were measured to assess and correct for the oxide interferences $^{139}La+^{16}O=^{155}Gd$, $^{140}Ce+^{16}O=^{156}Gd$ and $^{150}Nd+^{16}O=^{166}Er$. Data were processed in Iolite 2.5 using Si as an internal standard (Paton et al., 2011; Woodhead et al., 2007). Silicon contents were measured by calibrated energy-dispersive spectroscopy (EDS) in a Hitachi 4300 SE/N field emission scanning electron microscope equipped with an Oxford Instruments INCA X-MAX system. The primary reference material was NIST-610 using GeoReM recommended values from Jochum et al. (2011). Analyses of zircon with Ca > 50 ppm were excluded as being contaminated because of the extreme incompatibility of this element (Burnham and Berry, 2012). Chondrite normalization values were taken from O'Neill (2016). Analytical results are available in the supplementary online information.

X-ray absorption spectra at the Pr L_3-edge (5964 eV) were collected in fluorescence mode using a 100-element germanium array detector (Canberra Industries) at the XAS beamline at the Australian Synchrotron. The excitation energy was selected using a Si(111) double crystal monochromator, which was calibrated at the Cr-K absorption edge using an inline Cr metal foil (first maximum of the first derivative at 5989 eV).

Samples were analysed with a count time of 4 seconds for each energy step, with 3 eV steps in the pre-edge region of the XAS spectra (5764–5944 eV), 0.25 eV steps in the XANES region (5944–6014 eV), and in the EXAFS region spectra were collected in steps of 0.2 k to a maximum of 8 k (6209 eV).

The X-ray beam was focused at a glass harmonic rejection mirror upstream of the sample, and slits (0.2 mm horizontal, 0.3 mm vertical) were used to reduce the beam size to a ≈1 mm spot at the sample. A mask of 50 µm thick aluminium foil was applied to the front of the sample, with a small window cut around the area of interest (approximately 2 mm high, 3 mm wide). Scans were conducted at ten locations within this area.

Reference materials were (1) commercially available Pr_6O_{11} powder (Aldrich, 99.9%) diluted to ~2000 ppm Pr by mixing with BN, and (2) silicate glass containing ~5000 ppm each of La and Pr^{3+} prepared by mixing the above-mentioned Pr_6O_{11} powder, La_2O_3 (BDH, 99.9%) and a eutectic CMAS silicate composition, followed by melting in a graphite crucible at 1500 °C for 20 minutes and quenching in air. Data was pre-processed using the in-house Sakura program and the Athena program was used for background subtraction and edge-height normalization (Ravel and Newville, 2005).

This is the peer-reviewed, final accepted version for American Mineralogist, published by the Mineralogical Society of America.
The published version is subject to change. Cite as Authors (Year) Title. American Mineralogist, in press.
DOI: https://doi.org/10.2138/am-2020-7325. http://www.minsocam.org/

Results

Zircon

The zircon synthesis experiments produced crystals with similar shapes and sizes to those reported in Burnham and Berry (2012). The ratios of zircon/melt partition coefficients between the oxidized run (PtO_2) and reduced run (graphite), which we define as the parameter $\Delta\sim$, are given in Figure 2. As expected, there is a strong positive Ce-anomaly, with Ce enriched by a factor of ~100 in the oxidized experiment (where Ce^{4+} comprises a significant fraction of Ce) relative to the reduced experiment (almost exclusively Ce^{3+}). Likewise, Eu is more compatible in zircon in oxidized conditions (as Eu^{3+}) relative to reduced conditions (wither a higher proportion as Eu^{2+}). The non-redox sensitive REE should plot as a horizontal line at $\Delta\sim=1$, as they are not influenced by the oxygen buffer. Their deviation from unity is likely to result from zircon sector-zoning (Burnham and Berry, 2012). Praseodymium plots slightly above its expected position on a La–Nd interpolation line (hereafter Pr*, where $Pr^* = \sqrt[3]{(La \times Nd^2)}$ on a chondrite-normalized basis), but this enrichment is not completely resolved from the measurement uncertainty and so there is no evidence for Pr^{4+} at the high-temperature, high-fO_2 conditions of this experiment.

Stetindite-(Ce)

We measured REE patterns of stetindite-(Ce) from two localities: the type locality at Stetind pegmatite in Tysfjord, Norway (Fig. 3a; Schlüter et al., 2009), and the second known occurrence at Nolans Bore, Northern Territory, Australia (Fig. 3b; Anenburg et al., 2018; Huston et al., 2016).

Stetindite-(Ce) from Stetind (Fig. 4a) shows a positive Pr-anomaly (evident by Pr plotting higher than the expected position at Pr*). This anomaly is negligible in the most LREE-rich analyses, but becomes more significant with decreasing LREE, reaching a ~30% enrichment in the most LREE-poor stetindite-(Ce). These LREE-poor stetindite-(Ce) occur as fine-

grained feather-like coating on the LREE-rich, euhedral, stetindite-(Ce) (Schlüter et al., 2009).

Stetindite-(Ce) from Nolans Bore shows an apparent positive Pr-anomaly (Fig. 4b), but it might be misleading as it is an alteration phase of fluorapatite, which commonly exhibits curved LREE patterns with a maximum at Pr (Anenburg et al., 2018; Schoneveld et al., 2015). Therefore, REE contents from the Nolans Bore stetindite-(Ce) has been normalized to the average precursor unaltered fluorapatite (Fig. 5a), which modifies the shape of the pattern but nevertheless reveals a positive Pr-anomaly representing ~10% enrichment over Pr*. An as-yet-undescribed La-rich silicate–phosphate (Fig 3c; see Anenburg et al., 2018), which occurs in association with stetindite-(Ce), exhibits a complementary negative Ce anomaly (Fig. 4c). When normalized to the precursor unaltered fluorapatite, it additionally exhibits a negative Pr-anomaly amounting to a ~30% depletion relative to Pr* (Fig. 5b). The morphology of the Nolans Bore stetindite-(Ce) is anhedral, but the associated La-silicate–phosphate shows a fine-grained boytroidal habit characteristic of supergene environments (Anenburg et al., 2018).

XANES spectra obtained for the stetindite-(Ce) sample from Stetind, Norway, is given in Figure 6 together with reference spectra for Pr^{4+}-containing material (Pr_6O_{11}) and Pr^{4+}-absent material (silicate glass). A hump-like feature in the Pr^{4+} region is clearly observed in the stetindite-(Ce) spectrum. This is the first spectroscopic evidence for Pr^{4+} in a naturally occurring material.

Cerianite-(Ce)

A REE pattern of cerianite-(Ce) from Kerimasi, Tanzania (Zaitsev et al., 2011) is given in Fig. 7a. As expected, it is dominated by Ce, whereas the rest of the pattern is mostly flat, varying by less than a factor of two. Nonetheless, Pr plots above the rest of the trivalent REE.

Kerimasi is a carbonatite volcano, and like the carbonatite-related Nolans Bore (Anenburg and Mavrogenes, 2018; Anenburg et al., 2020), it is possible that the Pr-enrichment results from a curved LREE pattern. However, none of the published REE patterns of Kerimasi rocks and minerals show any curvature (Church, 1996; Guzmics et al., 2015). Zaitsev et al. (2011) interpreted the Kerimasi cerianite-(Ce) as alteration of apatite, but REE analyses of Kerimasi apatite given by Chakhmouradian et al. (2017) show a consistently decreasing REE pattern from La to Nd (Fig. 7a). Therefore, the positive Pr-anomaly observed in the Kerimasi cerianite-(Ce) pattern does not represent inherited curvature, but instead represents a true enrichment.

REE patterns of an additional cerianite-(Ce) from Sushina Hill, India (Chakrabarty et al., 2013) show a clear positive Pr-anomaly (Fig. 7b). Like Kerimasi, there is no evidence for a pre-existing LREE curvature from which the anomaly can be inherited (Chakrabarty et al., 2018).

Dyrnaesite-(La)

Dyrnaesite-(La) compositions given by Rønsbo et al. (2017) are given in Fig. 8. Even though it reportedly contains quadrivalent Ce (Balić-Žunić, 2017), no Ce anomaly is observed. Therefore, dyrnaesite-(La) cannot contain a Pr-anomaly, since in any case it would be much weaker than that of Ce.

Discussion

The above results show that small positive Pr anomalies accompany the Ce^{4+} minerals cerianite-(Ce) and stetindite-(Ce). Moreover, a negative Pr anomaly was found in a Ce-free mineral coexisting with stetindite-(Ce) in Nolans Bore. Synthetic zircon at extremely oxidizing conditions did not have an obvious Pr anomaly.

Our XANES spectra show that the white line is narrower and more intense in our stetindite-(Ce) samples than in the Pr-doped glasses (Fig. 6). This is likely due to the smaller number of local environments around Pr in the mineral structure than in the silicate glass. As a result, the absolute peak height at the energy that is characteristic of Pr^{3+} is not a reliable indicator of the redox state of Pr when comparing between materials with such different structures. The feature in the stetindite-(Ce) spectrum at 5982 eV is similar to that observed in the mixed-valence oxide Pr_6O_{11}, and is characteristic of Pr^{4+} (Dumschat et al., 1995; Ocaña et al., 1998; Ogier et al., 2019). The slight shift of the position of the Pr^{4+} peak between Pr_6O_{11} and stetindite-(Ce) is not considered significant; This feature has been observed to shift by ~2.5 eV between $PrBaO_3$ and PrO_2, attributed to crystal field effects (Dumschat et al., 1995). Similar differences are noted in the XANES spectra for Ce, in which the two characteristic peaks of Ce^{4+} vary in energy by 0.8–0.9 eV, and in their relative intensities, between reference compounds (Takahashi et al., 2002; Trail et al., 2015). The few, comparatively broad features in these XANES spectra are known to arise from a large number of transitions from $2p_{3/2}$ to 5d orbitals that are highly sensitive to the electronic configuration of the lanthanide atom, and not just oxidation state (Kvashnina et al., 2011; Suzuki et al., 2009).

Although the overlap of the La L_2-edge with the Pr L_3-edge could conceivably result in EXAFS oscillations from La appearing in the region of the Pr^{4+} peak, the complete absence of any such features in the spectrum of the La–Pr^{3+}-doped glass indicates that this is not an adequate explanation for our observations (Fig. 6).

Praseodymium oxidation can be formulated as:

$$Pr_2^{3+}O_3 + 0.5O_2 = 2Pr^{4+}O_2 \quad (1)$$

Thus, the presence of Pr^{4+} is preferred at higher oxygen fugacities (fO_2). Additionally, high temperature stabilizes the higher entropy side of the reaction (with the O_2 component),

promoting Pr^{3+}. Therefore, Pr^{4+} is strongly preferred at oxidizing, low-temperature conditions. This is in agreement with the observation of a Pr-anomaly in supergene formation environments of cerianite-(Ce) and Pr-anomalous stetindite-(Ce). In contrast, Pr^{4+} is unlikely to be stable at igneous temperatures, even at oxidizing conditions. The graphite-buffered run is equilibrated at conditions that closely approach FMQ, in which all Pr is trivalent. The Pt–PtO_2 oxygen buffer with which our synthetic zircons equilibrated is not quantitatively calibrated yet, but it is known to be more oxidizing than Ir–IrO_2, the most oxidizing solid-state oxygen buffer known so far (fO_2 = ~12 bar at 1300 °C and 1 atm, or 60 times more oxidizing than air; Belonoshko and Saxena (1991)) and close to the fugacity of pure supercritical O_2 at 1 GPa ($fO_2 = 10^{4.73}$ bar at 1300 °C). Evidently, at this combination of temperature and fO_2, no statistically significant Pr-anomaly was observed. Since such oxidizing conditions are unrealistically high for any plausible igneous process on Earth or elsewhere in the solar system, we conclude that Pr^{4+} is not stable in any high-temperature igneous conditions.

Lessons from materials science—zircon

Praseodymium-doped zircon is an excellent yellow pigment, noted for its brilliant color and thermal stability (Badenes et al., 2002; Chen et al., 2018; Montoya et al., 2011). The yellow color results from crystal field splitting (Kar et al., 2005), where Pr^{4+} substitutes Zr^{4+} on the dodecahedral site (Hill et al., 2000; Trojan, 1988). The existence of this mixed $(Zr,Pr^{4+})SiO_4$ compound seems to be at odds with our failure to incorporate Pr^{4+} in our experimental zircons, but there are several factors that appear to stabilize it.

Suitable combination of temperature and fO_2. Pr-bearing zircons are usually prepared in temperatures below 1100 °C, sometimes as low at 750 °C (Chen et al., 2018). Oxygen fugacity is buffered to atmospheric oxygen ($fO_2 = 10^{-0.7}$ bar), so lower temperatures cause the zircon synthesis to occur at conditions more oxidizing relative to a specific buffer. For

example, at 1000 °C, fO_2 of Ir–IrO_2 roughly equals that of air, and at 900 °C air is more oxidizing (fO_2 constrained by Ir–IrO_2 equals $10^{-1.59}$ bar). Therefore, under the assumption that Pr^{4+}/Pr^{3+} ratios are similar along a fO_2–temperature curve relative to an oxygen buffer, lower temperatures at a fixed atmospheric fO_2 will promote oxidation of Pr^{3+} to Pr^{4+}. Pr-zircons synthesized at high temperatures (> 1300 °C) lose some color or become green by reduction of Pr^{4+} to Pr^{3+}, which exsolves as a separate Pr^{3+} phase (e.g. $Pr^{3+}{}_4Si_3O_{12}$, $Pr^{3+}{}_2Si_2O_7$, $NaPr^{3+}{}_4(SiO_4)_3F$, or $Pr^{3+}{}_2Zr_2O_7$ (Badenes et al., 2002; Chen et al., 2018; Del Nero et al., 2004; Ocaña et al., 1999). Thus, the general observations stemming from reaction (1) hold in this case.

The use of sodic fluxes. Pr-doped zircons are prepared in the presence of a "mineralizer"—a flux that promotes the reaction between ZrO_2, SiO_2 and Pr_6O_{11}, and promotes crystallization. The most common flux is NaF, although other alkali or alkali-earth halides are occasionally used (Badenes et al., 2002; Chen et al., 2018; Del Nero et al., 2004; Hill et al., 2000; Ocaña et al., 1999; Ocaña et al., 1998). The commonly cited explanation for the mineralizer effectiveness is volatile transport of the reactants and lowering of crystallization temperature stabilizing Pr^{4+} (Badenes et al., 2002; Hill et al., 2000; Ocaña et al., 1999), but in the case of Pr-doped zircon an additional factor may be high optical basicity of the flux (Duffy, 1993; Moretti, 2005; Wagner, 1975). Cations with a high optical basicity (such as Na^+) tend to stabilize higher oxidation states of various metals as is often seen in silicate melts or solids (Anenburg and Le Losq, 2019; Balić-Žunić, 2017; Burnham and Berry, 2014; Ernst, 1962; Giuli et al., 2012; Markl et al., 2010). The cationic component of NaF is pure Na^+, maximizing the stabilization of Pr^{4+} relative to Pr^{3+}, making it available for incorporation into zircon.

Zirconium-bearing minerals in terrestrial peralkaline silicate melts do not contain any Pr anomalies. Agpaitic melts are usually equilibrated at reducing conditions (at values between

the IW and FMQ buffers; Marks and Markl, 2017), which are not sufficient to form Ce anomalies, let alone Pr anomalies, including in the hyperagpaitic Ce^{4+}-mineral dyrnaesite-(La) (Rønsbo et al., 2017). Zircons in nepheline syenites, on the other hand, contain some of the strongest Ce anomalies known from any igneous rock type, but no Pr anomalies (Belousova et al., 2002). Additionally, REE minerals formed in fluoride melt systems contain no anomalies (Vasyukova and Williams-Jones, 2016), or very weak Ce anomalies (Kynicky et al., 2019). Thus, stabilization by Na^+ is unlikely to affect the oxidation state of Pr in natural systems, because fO_2 is not as high as that reached when preparing synthetic Pr-zircon pigments.

Considering the combined effect of temperature, atmospheric fO_2, and stabilization by Na^+, it is not surprising that Pr^{4+} can be incorporated into synthetic zircon. However, these zircons usually contain a mix of both Pr^{3+} and Pr^{4+} (Badenes et al., 2002; Chen et al., 2018; Del Nero et al., 2004; Guo et al., 2018; Montoya et al., 2011; Ocaña et al., 1998), indicating incomplete oxidation of Pr. For example, Guo et al. (2018) showed miscibility of up to 9% $Ce^{4+}SiO_4$ into zircon, but Pr also exists in a separate $NaPr^{3+}F_4$ phase when Pr>2%. As Pr^{4+} has a smaller ionic radius, closer to Zr^{4+} than Ce^{4+}, it is expected to be even more compatible in zircon than Ce^{4+}. Therefore, the formation of $NaPrF_4$ suggests an abundance of Pr^{3+} in Pr-zircon formation systems. The absence of other Pr^{4+} phases from such experiments suggests that the incorporation of quadrivalent Pr into zircon may be promoted by crystal chemical effects, but limited by the overall Pr^{4+}/Pr^{3+} at these fO_2 conditions.

Lessons from materials science—cerium and praseodymium oxides

Cerium oxide (ceria: $Ce^{4+}O_2$ and its natural analogue cerianite-(Ce)) and praseodymium oxide (Pr_6O_{11}, or $PrO_{1.83}$) adopt fluorite-like structures (Borchert et al., 2008; Burnham and Eyring, 1968; Graham, 1955; Hull et al., 2009; Matović et al., 2013; Yashima et al., 2006), which differs from the hexagonal or monoclinic crystal structures typical for other trivalent

REE (including $Ce^{3+}_2O_3$). In moderately reducing conditions, which are not sufficient to form the ultra-reduced hexagonal Ce_2O_3, ceria adopts a lower symmetry crystal structure and becomes a mixed Ce^{4+}–Ce^{3+} oxide with the general formula CeO_{2-x} ($0 \leq x \leq 0.25$), where the lower valence Ce^{3+} is charge balanced by oxygen vacancies (Hull et al., 2009; Matsukawa et al., 2018; Ray et al., 1975; Sørensen, 1976). The stable form of Pr-oxide (Pr_6O_{11}) similarly contains oxygen vacancies (Sinev et al., 1996). Stabilization of pure PrO_2 requires strong oxidants, and it will readily revert to Pr_6O_{11} (Sieglaff and Eyring, 1957; Yidong and Yuan, 1980). Both Ce and Pr oxides (including intermediate solid solutions) are highly reactive and will readily gain or lose the oxygen vacancies (Gazulla et al., 2019; Hyde et al., 1966), leading to their many industrial applications as catalysts (Artini, 2018; Borchert et al., 2008).

As both CeO_2 and Pr_6O_{11} adopt closely-related crystal structures and contain similarly sized cations with the same valence and close electronic properties, they can form solid solutions (Chun et al., 2006; Ftikos et al., 1993; Knauth and Tuller, 1999; Logan and Shelef, 1994; Michel et al., 2017; Stefanik and Tuller, 2004; Takasu et al., 1984). Knauth and Tuller (1999) studied a mixed $Pr_{0.7}Ce_{0.3}O_{2-x}$ oxide between 470 and 640 °C and fO_2 of 0.2 to 10^{-3} and found that Ce was tetravalent in all conditions, but the Pr^{4+}/Pr^{3+} ratio (manifested by oxygen vacancies) was increasing with higher fO_2 and lower temperatures. Pr^{4+}/Pr^{3+} in these oxides is positively correlated with $1/T$ (Knauth and Tuller, 1999; Stefanik and Tuller, 2004), meaning that lowering temperature stabilizes Pr^{4+} at a rate that is enhanced at lower temperatures. The speciation is also affected by kinetic effects and cooling rate (Gazulla et al., 2019).

Because trivalent Ce or Pr can substitute in the $(Ce,Pr)O_2$ structure, charge balanced by oxygen vacancies, other trivalent REE such as La, Nd, Sm, etc. can likewise be accommodated (Artini, 2018; Biswas et al., 1997; Chockalingam et al., 2014; Lin et al., 2015). This leads to a two-fold mechanism for Pr incorporation in CeO_2. First, Pr will partition to CeO_2 as part of a smoothly changing partitioning pattern for all REE^{3+}. However,

this will not cause an anomaly to form. An anomaly requires a second mechanism: the presence of Pr^{4+} in the fluid the mineral is crystallizing from. The amount does need not be large if one oxidation state is much more compatible than the other. For instance, Burnham and Berry (2012) showed that Ce^{4+}/Ce^{3+}=0.0001 in the melt was sufficient to produce a measurable Ce anomaly in zircon, a mineral which strongly partitions Ce^{4+}. Therefore, a small amount of Pr^{4+} in the crystallizing medium should be sufficient to form a Pr anomaly in cerianite-(Ce) or stetindite-(Ce), minerals that presumably strongly partition Pr^{4+}.

Stabilization of Pr^{4+} in fluids

In order to preferentially partition Pr to Ce^{4+}-minerals relative to other REE, some amount of Pr^{4+} has to exist in the fluid the minerals are crystallizing from. This was empirically observed by the Pr anomalies detected in cerianite-(Ce) and stetindite-(Ce) (Fig. 5, 7).

In general, it is more difficult to stabilize REE^{4+} in solutions than it is in solids. For example, Heidt and McMillan (1954) succeeded in converting only 0.14% of Ce^{3+} to Ce^{4+} by photochemical oxidation in an oxidizing perchlorate solution. Praseodymium is more challenging, because Pr^{4+} has an oxidation potential high enough to decompose H_2O to O_2 and H_2 (Nugent et al., 1973). Nonetheless, Pr^{4+} has been stabilized in water for periods of milliseconds by pulse radiolysis (Faraggi and Feder, 1972), or for longer by electrochemical oxidation in an alkaline solution (Hobart et al., 1980). These decomposition reactions are kinetically controlled, and trace amounts of Pr^{4+} might persist for long enough to cause Pr anomalies in Ce^{4+}-dominant minerals.

Formation of Pr-dominant minerals

Because Pr is approximately an order of magnitude less abundant than neighboring Ce or Nd (Rudnick and Gao, 2014), making a Pr-dominant mineral by regular REE fractionating methods requires an unlikely REE pattern with a strong curvature and maximum at Pr, ideally

mixed with a negative Ce anomaly (Anenburg, 2020). Although the lower-abundance REE sometimes end up as the dominant element (e.g., monazite-(Sm), florencite-(Sm), samarskite-(Yb) or xenotime-(Yb); Buck et al., 1999; Masau et al., 2002; Repina et al., 2011; Simmons et al., 2006), the necessary enrichment factor for Pr over Nd is unprecedented (Anenburg, 2020). Nevertheless, the quadrivalent oxidation state of Pr opens a pathway for it to predominate in a mineral (e.g., Christy, 2015). To produce a Pr-dominant mineral, Ce would have to be removed first. Some minerals contain strong negative Ce anomalies, such as the La-silicate–phosphate found in Nolans Bore (Fig. 4c; Schoneveld et al., 2015), and former bridgmanite and "new aluminous phase" inclusions from Transition Zone diamonds (Thomson et al., 2016). However, these minerals are expected to be found adjacent to complementary Ce^{4+}-rich minerals that can absorb any Pr^{4+} that may form. Therefore, we suggest two paths that lead to Pr-mineral crystallization:

1. Differential sedimentary transport which physically separates the Ce-absent minerals from the rest. For example, the La-silicate–phosphate at Nolans Bore commonly resides in open cavities, whereas stetindite-(Ce) completely fills space. This could lead to preferential fragmentation of the rock during weathering along grain boundaries containing open cavities, releasing more Ce-depleted material to a sedimentary system. Strong oxidation at low temperatures could then cause exsolution of Pr^{4+} phases out of REE^{3+} minerals, similar to the formation cerianite-(Ce) exsolution out of REE-bearing apatite at Kerimasi (Zaitsev et al., 2011), or as demonstrated experimentally for monazite by Trail (2018).
2. Limited interaction with low temperature and oxidizing fluids could cause in-situ oxidation of Pr hosted in Ce-absent minerals. Too much interaction might mobilize the Pr into the adjacent Ce^{4+} minerals to form a solid solution. The transport fluid has to sustain oxidizing conditions long enough to separate Pr from its source, which can

be at the micrometer scale. The lifetime of Pr^{4+} in solutions is short (Suming and Rudong, 1983; Yidong and Yuan, 1980), so most likely any new minerals would be Pr^{3+} dominated. If the system retains its high oxidation state, it would be possible to form P_6O_{11} or another Pr^{4+} mineral. This becomes more likely in the presence of Na and F as they are known to stabilize Pr^{4+} compounds. For example, Asprey and Keenan (1961) synthesized crystalline $NaPrF_5$ and Na_2PrF_6 by reacting Na–Pr solutions and F_2 gas at 400 °C, and Mazej (2002) synthesized PrF_4 by reacting Pr_6O_{11} with UV-photolyzed F_2 gas at room temperature. Pure F_2 gas is unlikely to exist in nature, but it is possible that a less strong oxidizer can suffice to form these solid phases at lower temperatures.

Fluids containing Pr^{4+} may not even be required: Estevenon et al. (2019) demonstrated that, counterintuitively, low-temperature hydrothermal $CeSiO_4$ preferentially forms from Ce^{3+} precursors relative to Ce^{4+}. By analogy, the extreme difficulty of stabilizing Pr^{4+} in solution may not be a hindrance to formation of Pr^{4+}-bearing minerals, so long as the conditions are sufficiently cold and oxidizing to stabilize it in the solid state.

Terrestrial candidate–Atacama Desert, Chile

The Atacama in Chile is a dry desert plateau in which temperatures occasionally reach below 0 °C (Wörner et al., 2018b). It is host to many evolved granitoids (Wörner et al., 2018a), several of which contain elevated REE contents. The Mindat.org database lists several REE minerals known from the Atacama region: kimuraite-(Y), a hydrous carbonate; agardite-(Y), a hydrous arsenate (Morrison et al., 2013); florencite-(Ce) and florencite-(La), hydrous phosphates (Deyell et al., 2005); and most importantly, cerianite-(Ce). These minerals indicate REE exposure to supergene environments in the Atacama. Additionally, some hydrothermal ore deposits in Chile contain allanite, indicating some degree of REE mobility and enrichment (Marquardt et al., 2015; Rieger et al., 2010; Veloso et al., 2017). The

Atacama is well known for the occurrence of strong oxidizing salts: nitrates, perchlorates and iodates (Lybrand et al., 2016; Reich and Bao, 2018). The aridity of the Atacama can lead to conditions of metastable or local equilibrium, which could lead to separation of Ce-absent and other REE minerals, followed by formation of Pr-dominant minerals.

Are extraterrestrial Pr minerals possible?

A Pr-dominant mineral is likely to form from another REE-rich mineral precursor, and previous studies discussed the various degrees of REE-enrichments possible on other planetary bodies (Bonin, 2012; McLeod and Shaulis, 2018). However, as noted above, any detectable Pr^{4+} requires low temperatures and high fO_2, leading to Mars being the prime candidate. REE-minerals have been observed in Martian meteorites (Liu et al., 2016), and the Martian surface experienced prolonged low-temperature alteration under oxidizing conditions (Guitreau and Flahaut, 2019).

The Atacama surface conditions are commonly considered as analogues for the Martian surface (Lybrand et al., 2016), which contains all the basic ingredients which may be required for formation of Pr-dominant minerals. Recent observations suggest the presence of felsic or fractionated magmatism on Mars (Cousin et al., 2017; Meslin et al., 2013; Sautter et al., 2014; Wray et al., 2013), which could lead to local REE enrichment sufficient to form REE minerals. Additionally, oxidizing salts were detected by the Phoenix Lander and Curiosity Rover (Clark and Kounaves, 2016; Hecht et al., 2009; Leshin et al., 2013; Ming et al., 2014; Stern et al., 2015) and in Martian meteorites (Kounaves et al., 2014). The temperature of the Martian surface is lower than that of Earth, and it has abundant evidence for the former flow of liquid water. Low-temperature hydrothermal alteration of relatively evolved potassic rocks was observed by Curiosity (Thompson et al., 2016). Therefore, it possible that at some point in the Martian geological history a REE-rich mineral was exposed to oxidizing brines on the surface (e.g., Gough et al., 2011; Quinn et al., 2013), which allowed fractionation of Ce,

414 followed by another fractionation of Pr with the outcome of producing a Pr-dominant
415 mineral.

416 **A note on terbium**

417 Like Pr, Tb is also stable as a mixed-valance oxide Tb_4O_7 ($2Tb^{4+}O_2 \cdot Tb_2^{3+}O_3$). However, due
418 its low chondritic abundance and moderate compatibility, it does not reach levels which can
419 be analyzed precisely by EPMA. Furthermore, Tb has only one isotope: ^{157}Tb, which has an
420 oxide interference from $^{141}Pr^{16}O$, increasing uncertainty and obscuring any possible
421 anomalies when analyzed by mass spectrometry. Finally, Tb_4O_7 has Tb^{4+}/Tb^{3+} of 2, whereas
422 Pr_6O_{11} has Pr^{4+}/Pr^{3+} of 4. Taken together with the higher 4th ionization energy for Tb
423 compared to Pr (3839 and 3761 kJ/mol, respectively), the stability of Tb^{4+} is expected to be
424 lower than Pr^{4+}. Therefore, any Tb anomalies would be smaller in magnitude and more
425 challenging to detect.

426 **Implications**

427 Praseodymium anomalies are unlikely to exist in any high temperature igneous, metasomatic,
428 or hydrothermal process on Earth, or elsewhere in the solar system. Praseodymium anomalies
429 only become apparent in low temperature and oxidizing conditions. Stetindite-(Ce) from
430 Stetind only exhibits the Pr anomalies on supergene late-stage coating on pegmatitic
431 stetindite-(Ce), and Pr-anomalous stetindite-(Ce) from Nolans Bore coexists with a La-
432 silicate–phosphate of supergene origin. The fact that Pr-dominant minerals have not been
433 found in close to 100 known localities of cerianite-(Ce) and in the two known stetindite-(Ce)
434 localities puts a strong doubt on the existence of Pr-dominated minerals on Earth.

435 Other than earth, the only other solar system body with conditions conducive to the presence
436 of Pr^{4+} is Mars. With its overall low temperature and local accumulations of perchlorate, it is
437 possible that Pr^{4+} exists or has existed in the past on the surface of Mars. However,

enrichment of Pr such that it will become abundant enough to form its own mineral, and dominate relative to Ce requires (1) fractionated, REE-rich igneous rocks, (2) supergene alteration and formation of Ce-free and Ce^{4+} minerals, (3) separation of the two types of minerals by sedimentary processes, and (4) strong oxidation of the Ce-free minerals. It is extremely unlikely for all four processes to have occurred on same place on Mars, thus we doubt the presence of Pr-dominated minerals on Mars.

Acknowledgements

We express our gratitude to Tomas Husdal for providing us with the Stetind sample. This work was supported by Australian Research Council grant FL130100066. We acknowledge the facilities of Microscopy Australia at the Centre for Advanced Microscopy, The Australian National University. Laura Crisp and Charlotte Allen are thanked for their assistance with the LA-ICP-MS analyses. Part of this research was undertaken on the XAS beamline (12IDB) at the Australian Synchrotron through proposal ID 15793. We thank Shaunna Morrison, Daniel Hummer, and Martin P. Smith for peer reviews. Andrew G. Christy inspired this study.

References

Anenburg, M. (2020) Rare earth mineral diversity controlled by REE pattern shapes. Mineralogical Magazine in review.

Anenburg, M., Burnham, A.D., and Mavrogenes, J.A. (2018) REE redistribution textures in altered fluorapatite: symplectites, veins and phosphate-silicate-carbonate assemblages from the Nolans Bore P-REE-Th deposit, NT, Australia. The Canadian Mineralogist, 56, 331–354.

Anenburg, M., and Le Losq, C. (2019) Perrhenate sodalite growth from alkali silicate melts by noble metal catalysis. SN Applied Sciences, 1, 372.

Anenburg, M., and Mavrogenes, J.A. (2018) Carbonatitic versus hydrothermal origin for fluorapatite REE-Th deposits: Experimental study of REE transport and crustal "antiskarn" metasomatism. American Journal of Science, 318, 335–366.

Anenburg, M., Mavrogenes, J.A., and Bennett, V.C. (2020) The fluorapatite P-REE-Th vein deposit at Nolans Bore: genesis by carbonatite metasomatism. Journal of Petrology.

Artini, C. (2018) Rare-earth-doped ceria systems and their performance as solid electrolytes: A puzzling tangle of structural issues at the average and local scale. Inorganic Chemistry, 57, 13047–13062.

Asprey, L.B., and Keenan, T.K. (1961) Tetravalent lanthanides—I Sodium praseodymium(IV) fluorides. Journal of Inorganic and Nuclear Chemistry, 16, 260–262.

Badenes, J.A., Vicent, J.B., Llusar, M., Tena, M.A., and Monrós, G. (2002) The nature of Pr-$ZrSiO_4$ yellow ceramic pigment. Journal of Materials Science, 37, 1413–1420.

Balić-Žunić, T. (2017) The crystal structure of the new mineral dyrnaesite-(La),$Na_8Ce^{IV}REE_2(PO_4)_6$. Mineralogical Magazine, 81, 199–208.

Belonoshko, A., and Saxena, S.K. (1991) A molecular dynamics study of the pressure-volume-temperature properties of supercritical fluids: II. CO_2, CH_4, CO, O_2, and H_2. Geochimica et Cosmochimica Acta, 55, 3191–3208.

Belousova, E.A., Griffin, W.L., O'Reilly, S.Y., and Fisher, N.I. (2002) Igneous zircon: trace element composition as an indicator of source rock type. Contributions to Mineralogy and Petrology, 143, 602–622.

Biswas, R.G., Hartridge, A., Mallick, K.K., and Bhattcharaya, A.K. (1997) Preparation, structure and electrical conductivity of $Pr_{1-x}La_xO_{2-\delta}$ (x = 0.05, 0.1, 0.2). Journal of Materials Science Letters, 16, 1089–1091.

Bonin, B. (2012) Extra-terrestrial igneous granites and related rocks: A review of their occurrence and petrogenesis. Lithos, 153, 3–24.

Borchert, Y., Sonström, P., Wilhelm, M., Borchert, H., and Bäumer, M. (2008) Nanostructured praseodymium oxide: Preparation, structure, and catalytic properties. The Journal of Physical Chemistry C, 112, 3054–3063.

Buck, H.M., Cooper, M.A., Černý, P., Grice, J.D., and Hawthorne, F.C. (1999) Xenotime-(Yb), $YbPO_4$, a new mineral species from the Shatford Lake pegmatite group, southeastern Manitoba, Canada. The Canadian Mineralogist, 37, 1303–1306.

Burnham, A.D., and Berry, A.J. (2012) An experimental study of trace element partitioning between zircon and melt as a function of oxygen fugacity. Geochimica et Cosmochimica Acta, 95, 196–212.

-. (2014) The effect of oxygen fugacity, melt composition, temperature and pressure on the oxidation state of cerium in silicate melts. Chemical Geology, 366, 52–60.

Burnham, A.D., Berry, A.J., Halse, H.R., Schofield, P.F., Cibin, G., and Mosselmans, J.F.W. (2015) The oxidation state of europium in silicate melts as a function of oxygen fugacity, composition and temperature. Chemical Geology, 411, 248–259.

Burnham, D.A., and Eyring, L. (1968) Phase transformations in the praseodymium oxide-oxygen system: high-temperature X-ray diffraction studies. The Journal of Physical Chemistry, 72, 4415–4424.

Chakhmouradian, A.R., Reguir, E.P., Zaitsev, A.N., Couëslan, C., Xu, C., Kynický, J., Mumin, A.H., and Yang, P. (2017) Apatite in carbonatitic rocks: Compositional variation, zoning, element partitioning and petrogenetic significance. Lithos, 274–275, 188–213.

Chakrabarty, A., Mitchell, R.H., Ren, M., Pal, S., Pal, S., and Sen, A.K. (2018) Nb–Zr–REE re-mobilization and implications for transitional agpaitic rock formation: Insights from the Sushina Hill Complex, India. Journal of Petrology, 59, 1899–1938.

Chakrabarty, A., Mitchell, R.H., Ren, M., Sen, A.K., and Pruseth, K.L. (2013) Rinkite, cerianite-(Ce), and hingganite-(Ce) in syenite gneisses from the Sushina Hill Complex, India: occurrence, compositional data and petrogenetic significance. Mineralogical Magazine, 77, 3137–3153.

Chen, T., Zha, J., Zhang, X., Hu, X., Jiang, W., Xie, Z., and Jiang, W. (2018) Synthesis and characterization of $Pr_xZr_{1-x}SiO_4$ ($x = 0–0.08$) yellow pigments via non-hydrolytic sol-gel method. Journal of the European Ceramic Society, 38, 4568–4575.

Chockalingam, R., Ganguli, A.K., and Basu, S. (2014) Praseodymium and gadolinium doped ceria as a cathode material for low temperature solid oxide fuel cells. Journal of Power Sources, 250, 80–89.

Christy, A.G. (2015) Causes of anomalous mineralogical diversity in the Periodic Table. Mineralogical Magazine, 79, 33–49.

Chun, W., Graham, G.W., Lupescu, J.A., McCabe, R.W., Koranne, M.M., and Brezny, R. (2006) Reducibility of catalyzed cerium–praseodymium mixed oxides. Catalysis Letters, 106, 95–100.

Church, A.A. (1996) The petrology of the Kerimasi Carbonatite Volcano and the carbonatites of Oldoinyo Lengai with a review of other occurrences of extrusive carbonatites, PhD thesis, p. 384. University of London.

Clark, B.C., and Kounaves, S.P. (2016) Evidence for the distribution of perchlorates on Mars. International Journal of Astrobiology, 15, 311–318.

Cousin, A., Sautter, V., Payré, V., Forni, O., Mangold, N., Gasnault, O., Le Deit, L., Johnson, J., Maurice, S., Salvatore, M., Wiens, R.C., Gasda, P., and Rapin, W. (2017) Classification of igneous rocks analyzed by ChemCam at Gale crater, Mars. Icarus, 288, 265–283.

Del Nero, G., Cappelletti, G., Ardizzone, S., Fermo, P., and Gilardoni, S. (2004) Yellow Pr-zircon pigments: The role of praseodymium and of the mineralizer. Journal of the European Ceramic Society, 24, 3603–3611.

Deyell, C.L., Rye, R.O., Landis, G.P., and Bissig, T. (2005) Alunite and the role of magmatic fluids in the Tambo high-sulfidation deposit, El Indio–Pascua belt, Chile. Chemical Geology, 215, 185–218.

Duffy, J.A. (1993) A review of optical basicity and its applications to oxidic systems. Geochimica et Cosmochimica Acta, 57, 3961–3970.

Dumschat, J., Wortmann, G., and Felner, I. (1995) $L_{II,III}$ near-edge study of tetravalent Pr-oxides: $PrBaO_3$ and PrO_2. Physica B: Condensed Matter, 208&209, 313–315.

Ernst, W.G. (1962) Synthesis, stability relations, and occurrence of riebeckite and riebeckite-arfvedsonite solid solutions. The Journal of Geology, 70, 689–736.

Estevenon, P., Welcomme, E., Szenknect, S., Mesbah, A., Moisy, P., Poinssot, C., and Dacheux, N. (2019) Preparation of $CeSiO_4$ from aqueous precursors under soft hydrothermal conditions. Dalton Transactions, 48, 7551–7559.

Faraggi, M., and Feder, A. (1972) Pulse radiolysis studies in lanthanide aqueous solutions. II. Formation, spectrum, and some chemical properties of praseodymium(IV) in aqueous solution. The Journal of Chemical Physics, 56, 3294–3297.

Ftikos, C., Nauer, M., and Steele, B.C.H. (1993) Electrical conductivity and thermal expansion of ceria doped with Pr, Nb and Sn. Journal of the European Ceramic Society, 12, 267–270.

Gazulla, M.F., Ventura, M.J., Andreu, C., Gilabert, J., Orduña, M., and Rodrigo, M. (2019) Praseodymium oxides. Complete characterization by determining oxygen content. Microchemical Journal, 148, 291-298.

Giuli, G., Alonso-Mori, R., Cicconi, M.R., Paris, E., Glatzel, P., Eeckhout, S.G., and Scaillet, B. (2012) Effect of alkalis on the Fe oxidation state and local environment in peralkaline rhyolitic glasses. American Mineralogist, 97, 468–475.

549 Gough, R.V., Chevrier, V.F., Baustian, K.J., Wise, M.E., and Tolbert, M.A. (2011) Laboratory studies of
550 perchlorate phase transitions: Support for metastable aqueous perchlorate solutions on Mars. Earth and
551 Planetary Science Letters, 312, 371–377.
552 Graham, A.R. (1955) Cerianite CeO_2: A new rare-earth oxide mineral. American Mineralogist, 40, 560–564.
553 Guitreau, M., and Flahaut, J. (2019) Record of low-temperature aqueous alteration of Martian zircon during the
554 late Amazonian. Nature Communications, 10, 2457.
555 Guo, D., Xie, M., Ma, N., Yang, Q., Luo, Z., Chu, Y., Zhang, Y., and Rao, P. (2018) Synthesis and
556 characterization of (Pr, Ce)-$ZrSiO_4$ ceramic pigments: The properties of the pigments and the effect of
557 Ce. Journal of the American Ceramic Society, 102, 2619–2628.
558 Guzmics, T., Zajacz, Z., Mitchell, R.H., Szabó, C., and Wälle, M. (2015) The role of liquid–liquid immiscibility
559 and crystal fractionation in the genesis of carbonatite magmas: insights from Kerimasi melt inclusions.
560 Contributions to Mineralogy and Petrology, 169, 17.
561 Hazen, R.M., and Ausubel, J.H. (2016) On the nature and significance of rarity in mineralogy. American
562 Mineralogist, 101, 1245–1251.
563 Hazen, R.M., Grew, E.S., Downs, R.T., Golden, J., and Hystad, G. (2015) Mineral ecology: chance and
564 necessity in the mineral diversity of terrestrial planets. The Canadian Mineralogist, 53, 295–324.
565 Hecht, M.H., Kounaves, S.P., Quinn, R.C., West, S.J., Young, S.M.M., Ming, D.W., Catling, D.C., Clark, B.C.,
566 Boynton, W.V., Hoffman, J., DeFlores, L.P., Gospodinova, K., Kapit, J., and Smith, P.H. (2009)
567 Detection of perchlorate and the soluble chemistry of Martian soil at the Phoenix Lander site. Science,
568 325, 64–67.
569 Heidt, L.J., and McMillan, A.F. (1954) Influence of perchloric acid and cerous perchlorate upon the
570 photochemical oxidation of cerous to ceric perchlorate in dilute aqueous perchloric acid. Journal of the
571 American Chemical Society, 76, 2135–2139.
572 Hill, K., Lehman, R., and Swiler, D. (2000) Effects of selected processing variables on color formation in
573 praseodymium-doped zircon pigments. Journal of the American Ceramic Society, 83, 2177–2182.
574 Hobart, D.E., Samhoun, K., Young, J.P., Norvell, V.E., Mamantov, G., and Peterson, J.R. (1980) Stabilization
575 of praseodymium(IV) and terbium(IV) in aqueous carbonate solution. Inorganic and Nuclear
576 Chemistry Letters, 16, 321–328.
577 Hull, S., Norberg, S.T., Ahmed, I., Eriksson, S.G., Marrocchelli, D., and Madden, P.A. (2009) Oxygen vacancy
578 ordering within anion-deficient Ceria. Journal of Solid State Chemistry, 182, 2815–2821.

579 Huston, D.L., Maas, R., Cross, A., Hussey, K.J., Mernagh, T.P., Fraser, G., and Champion, D.C. (2016) The
580 Nolans Bore rare-earth element-phosphorus-uranium mineral system: geology, origin and post-
581 depositional modifications. Mineralium Deposita, 51, 797–822.
582 Hyde, B.G., Bevan, D.J.M., and Eyring, L. (1966) On the praseodymium+oxygen system. Philosophical
583 Transactions of the Royal Society A: Mathematical, Physical and Engineering Sciences, 259, 583–614.
584 Ingrao, N.J., Hammouda, T., Boyet, M., Gaborieau, M., Moine, B.N., Vlastelic, I., Bouhifd, M.A., Devidal, J.-
585 L., Mathon, O., Testemale, D., Hazemann, J.-L., and Proux, O. (2019) Rare earth element partitioning
586 between sulphides and melt: Evidence for Yb^{2+} and Sm^{2+} in EH chondrites. Geochimica et
587 Cosmochimica Acta, 265, 182–197.
588 Jochum, K.P., Weis, U., Stoll, B., Kuzmin, D., Yang, Q., Raczek, I., Jacob, D.E., Stracke, A., Birbaum, K.,
589 Frick, D.A., Günther, D., and Enzweiler, J. (2011) Determination of reference values for NIST SRM
590 610–617 glasses following ISO guidelines. Geostandards and Geoanalytical Research, 35, 397–429.
591 Kar, J.K., Stevens, R., and Bowen, C.R. (2005) Processing and characterisation of Pr–zircon pigment powder.
592 Advances in Applied Ceramics, 104, 233–238.
593 Knauth, P., and Tuller, H.L. (1999) Nonstoichiometry and relaxation kinetics of nanocrystalline mixed
594 praseodymium–cerium oxide $Pr_{0.7}Ce_{0.3}O_{2-x}$. Journal of the European Ceramic Society, 19, 831–836.
595 Kounaves, S.P., Carrier, B.L., O'Neil, G.D., Stroble, S.T., and Claire, M.W. (2014) Evidence of martian
596 perchlorate, chlorate, and nitrate in Mars meteorite EETA79001: Implications for oxidants and
597 organics. Icarus, 229, 206–213.
598 Kvashnina, K.O., Butorin, S.M., and Glatzel, P. (2011) Direct study of the f-electron configuration in lanthanide
599 systems. Journal of Analytical Atomic Spectrometry, 26, 1265–1272.
600 Kynicky, J., Smith, M.P., Song, W., Chakhmouradian, A.R., Xu, C., Kopriva, A., Galiova, M.V., and Brtnicky,
601 M. (2019) The role of carbonate-fluoride melt immiscibility in shallow REE deposit evolution.
602 Geoscience Frontiers, 10, 527–537.
603 Leshin, L.A., Mahaffy, P.R., Webster, C.R., Cabane, M., Coll, P., Conrad, P.G., Archer, P.D., Atreya, S.K.,
604 Brunner, A.E., Buch, A., Eigenbrode, J.L., Flesch, G.J., Franz, H.B., Freissinet, C., Glavin, D.P.,
605 McAdam, A.C., Miller, K.E., Ming, D.W., Morris, R.V., Navarro-González, R., Niles, P.B., Owen, T.,
606 Pepin, R.O., Squyres, S., Steele, A., Stern, J.C., Summons, R.E., Sumner, D.Y., Sutter, B., Szopa, C.,
607 Teinturier, S., Trainer, M.G., Wray, J.J., and Grotzinger, J.P. (2013) Volatile, isotope, and organic
608 analysis of Martian fines with the Mars Curiosity Rover. Science, 341, 1238937.

Lin, X., Lü, Q., Zhu, L., and Liu, X. (2015) Synthesis and characterization of $Ce_{0.8}Sm_{0.2-x}Pr_xO_{2-\delta}$ (x=0.02–0.08) solid electrolyte materials. Journal of Rare Earths, 33, 411–416.

Liu, Y., Ma, C., Beckett, J.R., Chen, Y., and Guan, Y. (2016) Rare-earth-element minerals in martian breccia meteorites NWA 7034 and 7533: Implications for fluid–rock interaction in the martian crust. Earth and Planetary Science Letters, 451, 251–262.

Logan, A.D., and Shelef, M. (1994) Oxygen availability in mixed cerium/praseodymium oxides and the effect of noble metals. Journal of Materials Research, 9, 468–475.

Lybrand, R.A., Bockheim, J.G., Ge, W., Graham, R.C., Hlohowskyj, S.R., Michalski, G., Prellwitz, J.S., Rech, J.A., Wang, F., and Parker, D.R. (2016) Nitrate, perchlorate, and iodate co-occur in coastal and inland deserts on Earth. Chemical Geology, 442, 174–186.

Markl, G., Marks, M.A.W., and Frost, B.R. (2010) On the controls of oxygen fugacity in the generation and crystallization of peralkaline melts. Journal of Petrology, 51, 1831–1847.

Marks, M.A.W., and Markl, G. (2017) A global review on agpaitic rocks. Earth-Science Reviews, 173, 229–258.

Marquardt, M., Cembrano, J., Bissig, T., and Vázquez, C. (2015) Mid Cretaceous Cu-Au (Mo) mineralization in the Vallenar district: new Re-Os age constraints from Productora deposit, northern Chile. XIV Congreso Geológico Chileno, p. 421–424, La Serena.

Martin, R.L. (1974) Structural theory for non-stoicheiometry. Part I. Defect fluorite-type structures: lanthanoid oxides MO_x with $1.7 \leqslant x \leqslant 2.0$. Journal of the Chemical Society, Dalton Transactions, 1335–1350.

Masau, M., Černý, P., Cooper, M.A., Chapman, R., and Grice, J.D. (2002) Monazite-(Sm), a new member of the monazite group from the Annie Claim #3 granitic pegmatite, Southeastern Manitoba. The Canadian Mineralogist, 40, 1649–1655.

Matović, B., Pantić, J., Prekajski, M., Stanković, N., Bučevac, D., Minović, T., and Čebela, M. (2013) Synthesis and characterization of Pr_6O_{11} nanopowders. Ceramics International, 39, 3151–3155.

Matsukawa, T., Hoshikawa, A., and Ishigaki, T. (2018) Temperature-induced structural transition of ceria by bulk reduction under hydrogen atmosphere. CrystEngComm, 20, 4359–4363.

Mazej, Z. (2002) Room temperature syntheses of lanthanoid tetrafluorides (LnF_4, Ln = Ce, Pr, Tb). Journal of Fluorine Chemistry, 118, 127–129.

McLeod, C., and Shaulis, B. (2018) Rare earth elements in planetary crusts: Insights from chemically evolved igneous suites on Earth and the Moon. Minerals, 8, 455.

Meslin, P.-Y., Gasnault, O., Forni, O., Schröder, S., Cousin, A., Berger, G., Clegg, S.M., Lasue, J., Maurice, S., Sautter, V., Le Mouélic, S., Wiens, R.C., Fabre, C., Goetz, W., Bish, D., Mangold, N., Ehlmann, B., Lanza, N., Harri, A.-M., Anderson, R., Rampe, E., McConnochie, T.H., Pinet, P., Blaney, D., Léveillé, R., Archer, D., Barraclough, B., Bender, S., Blake, D., Blank, J.G., Bridges, N., Clark, B.C., DeFlores, L., Delapp, D., Dromart, G., Dyar, M.D., Fisk, M., Gondet, B., Grotzinger, J., Herkenhoff, K., Johnson, J., Lacour, J.-L., Langevin, Y., Leshin, L., Lewin, E., Madsen, M.B., Melikechi, N., Mezzacappa, A., Mischna, M.A., Moores, J.E., Newsom, H., Ollila, A., Perez, R., Renno, N., Sirven, J.-B., Tokar, R., de la Torre, M., d'Uston, L., Vaniman, D., and Yingst, A. (2013) Soil diversity and hydration as observed by ChemCam at Gale Crater, Mars. Science, 341, 1238670.

Michel, K., Eufinger, J.-P., Ulbrich, G., Lerch, M., Janek, J., and Elm, M.T. (2017) Combining two redox active rare earth elements for oxygen storage – electrical properties and defect chemistry of ceria–praseodymia single crystals. Physical Chemistry Chemical Physics, 19, 17661–17669.

Ming, D.W., Archer, P.D., Glavin, D.P., Eigenbrode, J.L., Franz, H.B., Sutter, B., Brunner, A.E., Stern, J.C., Freissinet, C., McAdam, A.C., Mahaffy, P.R., Cabane, M., Coll, P., Campbell, J.L., Atreya, S.K., Niles, P.B., Bell, J.F., Bish, D.L., Brinckerhoff, W.B., Buch, A., Conrad, P.G., Des Marais, D.J., Ehlmann, B.L., Fairén, A.G., Farley, K., Flesch, G.J., Francois, P., Gellert, R., Grant, J.A., Grotzinger, J.P., Gupta, S., Herkenhoff, K.E., Hurowitz, J.A., Leshin, L.A., Lewis, K.W., McLennan, S.M., Miller, K.E., Moersch, J., Morris, R.V., Navarro-González, R., Pavlov, A.A., Perrett, G.M., Pradler, I., Squyres, S.W., Summons, R.E., Steele, A., Stolper, E.M., Sumner, D.Y., Szopa, C., Teinturier, S., Trainer, M.G., Treiman, A.H., Vaniman, D.T., Vasavada, A.R., Webster, C.R., Wray, J.J., and Yingst, R.A. (2014) Volatile and organic compositions of sedimentary rocks in Yellowknife Bay, Gale Crater, Mars. Science, 343, 1245267.

Montoya, N., Herrera, G., and Alarcón, J. (2011) Synthesis and characterization of praseodymium-containing $ZrSiO_4$ solid solutions from gels. Ceramics International, 37, 3609–3616.

Moretti, R. (2005) Polymerisation, basicity, oxidation state and their role in ionic modelling of silicate melts. Annals of Geophysics, 48, 583–608.

Morrison, S.M., Domanik, K.J., Origlieri, M.J., and Downs, R.T. (2013) Agardite-(Y), $Cu^{2+6}Y(AsO_4)_3(OH)_6 \cdot 3H_2O$. Acta Crystallographica Section E, 69, i61–i62.

Nugent, L.J., Baybarz, R.D., Burnett, J.L., and Ryan, J.L. (1973) Electron-transfer and f–d absorption bands of some lanthanide and actinide complexes and the standard (II–III) oxidation potential for each member of the lanthanide and actinide series. The Journal of Physical Chemistry, 77, 1528–1539.

O'Neill, H.S.C. (2016) The smoothness and shapes of chondrite-normalized rare earth element patterns in basalts. Journal of Petrology, 57, 1463–1508.

Ocaña, M., Caballero, A., González-Elipe, A.n.R., Tartaj, P., Serna, C.J., and Merino, R.I. (1999) The effects of the NaF flux on the oxidation state and localisation of praseodymium in Pr-doped zircon pigments. Journal of the European Ceramic Society, 19, 641–648.

Ocaña, M., Caballero, A., González-Elípe, A.R., Tartaj, P., and Serna, C.J. (1998) Valence and localization of praseodymium in Pr-doped zircon. Journal of Solid State Chemistry, 139, 412–415.

Ogier, T., Prestipino, C., Figueroa, S., Mauvy, F., Mougin, J., Grenier, J.C., Demourgues, A., and Bassat, J.M. (2019) In-situ study of cationic oxidation states in $Pr_2NiO_{4+\delta}$ using X-ray absorption near-edge spectroscopy. Chemical Physics Letters, 727, 116–120.

Paton, C., Hellstrom, J., Paul, B., Woodhead, J., and Hergt, J. (2011) Iolite: Freeware for the visualisation and processing of mass spectrometric data. Journal of Analytical Atomic Spectrometry, 26, 2508–2518.

Quinn, R.C., Martucci, H.F.H., Miller, S.R., Bryson, C.E., Grunthaner, F.J., and Grunthaner, P.J. (2013) Perchlorate radiolysis on Mars and the origin of Martian soil reactivity. Astrobiology, 13, 515–520.

Ravel, B., and Newville, M. (2005) ATHENA, ARTEMIS, HEPHAESTUS: data analysis for X-ray absorption spectroscopy using IFEFFIT. Journal of Synchrotron Radiation, 12, 537–541.

Ray, S.P., Nowick, A.S., and Cox, D.E. (1975) X-ray and neutron diffraction study of intermediate phases in nonstoichiometric cerium dioxide. Journal of Solid State Chemistry, 15, 344–351.

Reich, M., and Bao, H. (2018) Nitrate deposits of the Atacama Desert: A marker of long-term hyperaridity. Elements, 14, 251–256.

Repina, S.A., Popova, V.I., Churin, E.I., Belogub, E.V., and Khiller, V.V. (2011) Florencite-(Sm)—$(Sm,Nd)Al_3(PO_4)_2(OH)_6$: A new mineral species of the alunite–jarosite group from the subpolar urals. Geology of Ore Deposits, 53, 564–574.

Rieger, A.A., Akker, B., Marschik, R., Díaz, M., Hölzl, S., Chiaradia, M., and Spangenberg, J.E. (2010) The hypogene iron oxide copper-gold mineralization in the Mantoverde district, northern Chile. Economic Geology, 105, 1271–1299.

Rønsbo, J.G., Balić-Žunić, T., and Petersen, O.V. (2017) Dyrnaesite-(La) a new hyperagpaitic mineral from the Ilímaussaq alkaline complex, South Greenland. Mineralogical Magazine, 81, 103–111.

Rudnick, R.L., and Gao, S. (2014) Composition of the continental crust. In R.L. Rudnick, Ed. Treatise on Geochemistry (Second Edition), Volume 4: The Crust, p. 1–51. Elsevier, Amsterdam.

Sautter, V., Fabre, C., Forni, O., Toplis, M.J., Cousin, A., Ollila, A.M., Meslin, P.Y., Maurice, S., Wiens, R.C., Baratoux, D., Mangold, N., Le Mouélic, S., Gasnault, O., Berger, G., Lasue, J., Anderson, R.A., Lewin, E., Schmidt, M., Dyar, D., Ehlmann, B.L., Bridges, J., Clark, B., and Pinet, P. (2014) Igneous mineralogy at Bradbury Rise: The first ChemCam campaign at Gale crater. Journal of Geophysical Research: Planets, 119, 30–46.

Schlüter, J., Malcherek, T., and Husdal, T.A. (2009) The new mineral stetindite, $CeSiO_4$, a cerium end-member of the zircon group. Neues Jahrbuch für Mineralogie - Abhandlungen, 186, 195–200.

Schoneveld, L., Spandler, C., and Hussey, K. (2015) Genesis of the central zone of the Nolans Bore rare earth element deposit, Northern Territory, Australia. Contributions to Mineralogy and Petrology, 170, 11.

Shannon, R.D. (1976) Revised effective ionic radii and systematic studies of interatomic distances in halides and chalcogenides. Acta Crystallographica Section A, 32, 751–767.

Sieglaff, C.L., and Eyring, L. (1957) Praseodymium oxides. IV. A study of the region $PrO_{1.83}$–$PrO_{2.00}$. Journal of the American Chemical Society, 79, 3024–3026.

Simmons, W.B., Hanson, S.L., and Falster, A.U. (2006) Samarskite-(Yb): A new species of the samarskite group from the Little Patsy pegmatite, Jefferson County, Colorado. The Canadian Mineralogist, 44, 1119–1125.

Sinev, M.Y., Graham, G.W., Haack, L.P., and Shelef, M. (1996) Kinetic and structural studies of oxygen availability of the mixed oxides $Pr_{1-x}M_xO_y$ (M = Ce, Zr). Journal of Materials Research, 11, 1960–1971.

Sørensen, O.T. (1976) Thermodynamic studies of the phase relationships of nonstoichiometric cerium oxides at higher temperatures. Journal of Solid State Chemistry, 18, 217–233.

Stefanik, T.S., and Tuller, H.L. (2004) Nonstoichiometry and defect chemistry in praseodymium-cerium oxide. Journal of Electroceramics, 13, 799–803.

Stern, J.C., Sutter, B., Freissinet, C., Navarro-González, R., McKay, C.P., Archer, P.D., Buch, A., Brunner, A.E., Coll, P., Eigenbrode, J.L., Fairen, A.G., Franz, H.B., Glavin, D.P., Kashyap, S., McAdam, A.C., Ming, D.W., Steele, A., Szopa, C., Wray, J.J., Martín-Torres, F.J., Zorzano, M.-P., Conrad, P.G., and

Mahaffy, P.R. (2015) Evidence for indigenous nitrogen in sedimentary and aeolian deposits from the *Curiosity* rover investigations at Gale crater, Mars. Proceedings of the National Academy of Sciences, 112, 4245–4250.

Suming, H., and Rudong, Y. (1983) The oxidation of trivalent praseodymium and terbium with ozone in aqueous ortho-tellurate solution. Chemical Journal of Chinese Universities, 4, 680–684.

Suzuki, C., Nishi, T., Nakada, M., Akabori, M., Hirata, M., and Kaji, Y. (2009) Calculation of the electronic structure of AmO_2 and Pr_6O_{11} for XANES analysis with redox property. International Journal of Quantum Chemistry, 109, 2744–2752.

Takahashi, Y., Sakami, H., and Nomura, M. (2002) Determination of the oxidation state of cerium in rocks by Ce L_{III}-edge X-ray absorption near-edge structure spectroscopy. Analytica Chimica Acta, 468, 345–354.

Takasu, Y., Sugino, T., and Matsuda, Y. (1984) Electrical conductivity of praseodymia doped ceria. Journal of Applied Electrochemistry, 14, 79–81.

Thompson, L.M., Schmidt, M.E., Spray, J.G., Berger, J.A., Fairén, A.G., Campbell, J.L., Perrett, G.M., Boyd, N., Gellert, R., Pradler, I., and VanBommel, S.J. (2016) Potassium-rich sandstones within the Gale impact crater, Mars: The APXS perspective. Journal of Geophysical Research: Planets, 121, 1981–2003.

Thomson, A.R., Kohn, S.C., Bulanova, G.P., Smith, C.B., Araujo, D., and Walter, M.J. (2016) Trace element composition of silicate inclusions in sub-lithospheric diamonds from the Juina-5 kimberlite: Evidence for diamond growth from slab melts. Lithos, 265, 108–124.

Trail, D. (2018) Redox-controlled dissolution of monazite in fluids and implications for phase stability in the lithosphere. American Mineralogist, 103, 453–461.

Trail, D., Tailby, N.D., Lanzirotti, A., Newville, M., Thomas, J.B., and Watson, E.B. (2015) Redox evolution of silicic magmas: Insights from XANES measurements of Ce valence in Bishop Tuff zircons. Chemical Geology, 402, 77–88.

Trojan, M. (1988) Synthesis of a yellow zircon pigment. Dyes and Pigments, 9, 261–273.

Vasyukova, O., and Williams-Jones, A.E. (2016) The evolution of immiscible silicate and fluoride melts: Implications for REE ore-genesis. Geochimica et Cosmochimica Acta, 172, 205–224.

Veloso, E., Cembrano, J., Arancibia, G., Heuser, G., Neira, S., Siña, A., Garrido, I., Vermeesch, P., and Selby, D. (2017) Tectono-metallogenetic evolution of the Fe–Cu deposit of Dominga, northern Chile. Mineralium Deposita, 52, 595–620.

Wagner, C. (1975) The concept of the basicity of slags. Metallurgical Transactions B, 6, 405–409.

Willauer, A.R., Palumbo, C.T., Fadaei-Tirani, F., Zivkovic, I., Douair, I., Maron, L., and Mazzanti, M. (2020) Accessing the +IV oxidation state in molecular complexes of praseodymium. Journal of the American Chemical Society, 142, 5538–5542.

Woodhead, J.D., Hellstrom, J., Hergt, J.M., Greig, A., and Maas, R. (2007) Isotopic and elemental imaging of geological materials by laser ablation inductively coupled plasma-mass spectrometry. Geostandards and Geoanalytical Research, 31, 331–343.

Wörner, G., Mamani, M., and Blum-Oeste, M. (2018a) Magmatism in the central Andes. Elements, 14, 237–244.

Wörner, G., Schildgen, T.F., and Reich, M. (2018b) The central Andes: Elements of an extreme land. Elements, 14, 225–230.

Wray, J.J., Hansen, S.T., Dufek, J., Swayze, G.A., Murchie, S.L., Seelos, F.P., Skok, J.R., Irwin Iii, R.P., and Ghiorso, M.S. (2013) Prolonged magmatic activity on Mars inferred from the detection of felsic rocks. Nature Geoscience, 6, 1013–1017.

Yashima, M., Kobayashi, S., and Yasui, T. (2006) Crystal structure and the structural disorder of ceria from 40 to 1497 °C. Solid State Ionics, 177, 211–215.

Yidong, G., and Yuan, S. (1980) Study of tetravalent praseodymium compounds—I—Preparation of Ce(IV)–Pr(IV) heteropolynuclear oxide at room temperature, and the behavior of tetravalent praseodymium in several acid solutions. Chemical Journal of Chinese Universities, 1, 1–13.

Zaitsev, A.N., Chakhmouradian, A.R., Siidra, O.I., Spratt, J., Williams, C.T., Stanley, C.J., Petrov, S.V., Britvin, S.N., and Polyakova, E.A. (2011) Fluorine-, yttrium- and lanthanide-rich cerianite-(Ce) from carbonatitic rocks of the Kerimasi volcano and surrounding explosion craters, Gregory Rift, northern Tanzania. Mineralogical Magazine, 75, 2813–2822.

Figure Captions

Figure 1. Ionic radii for cations of interest from Shannon (1976).

Figure 2. Ratios of zircon/melt REE partition coefficients for Pt–PtO_2 and graphite-buffered runs. Error bars indicate 1 sd of several analyses on zircon and glass, propagated through the division stages.

Figure 3. Backscattered electron images of (a) stetindite-(Ce) from Stetind, (b) stetindite-(Ce) from Nolans Bore, and (c) La-silicate–phosphate from Nolans Bore. Oval craters are laser ablation spots. Scale bar is 50 µm. Abbreviations: stet–stetinite-(Ce); stet*–supergene stetindite-(Ce); fap–fluorapatite; lsp–La-silicate–phosphate.

Figure 4. Chondrite-normalized REE patterns of (a) stetindite-(Ce) from Stetind, (b) stetindite-(Ce) from Nolans Bore, and (c) La-silicate–phosphate from Nolans Bore. Error bars indicate analytical uncertainty at 2 se. Uncertainties smaller than the symbol size are not plotted.

Figure 5. REE patterns of (a) stetindite-(Ce) and (b) La-silicate–phosphate, normalized to unaltered Nolans Bore fluorapatite. Error bars indicate 1 se of analytical uncertainty, propagated through division. Uncertainties smaller than the symbol size are not plotted.

Figure 6. XANES spectra of a mixed Pr^{3+}–Pr^{4+} oxide Pr_6O_{11}, a synthetic La–Pr^{3+} silicate glass, and stetindite-(Ce) from Stetind, Norway. The vertical gray band indicates the Pr^{4+}-peak region. The contribution of Pr^{4+} in stetindite-(Ce) is indicated by the arrow.

Figure 7. Chondrite-normalized REE patterns of cerianite-(Ce) from (a) Kerimasi, and (b) Sushina Hill. LREE patterns of unaltered Kerimasi apatite are shown for comparison. Dashed lines are interpolations for elements with no data available.

Figure 8. Chondrite-normalized LREE pattern of dyrnaesite-(La) from the type locality.

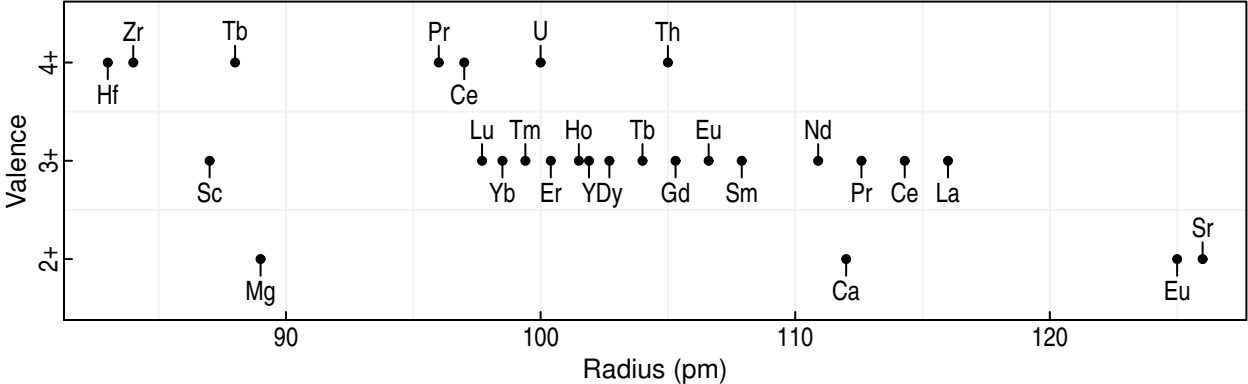
Valence
4+
3+
2+
Hf
Zr
Tb
Sc
Mg
Pr
Ce
U
Th
Lu
Yb
Tm
Er
Ho
YDy
Tb
Gd
Eu
Sm
Nd
Pr
Ce
La
Ca
Sr
Eu
90
100
110
120
Radius (pm)

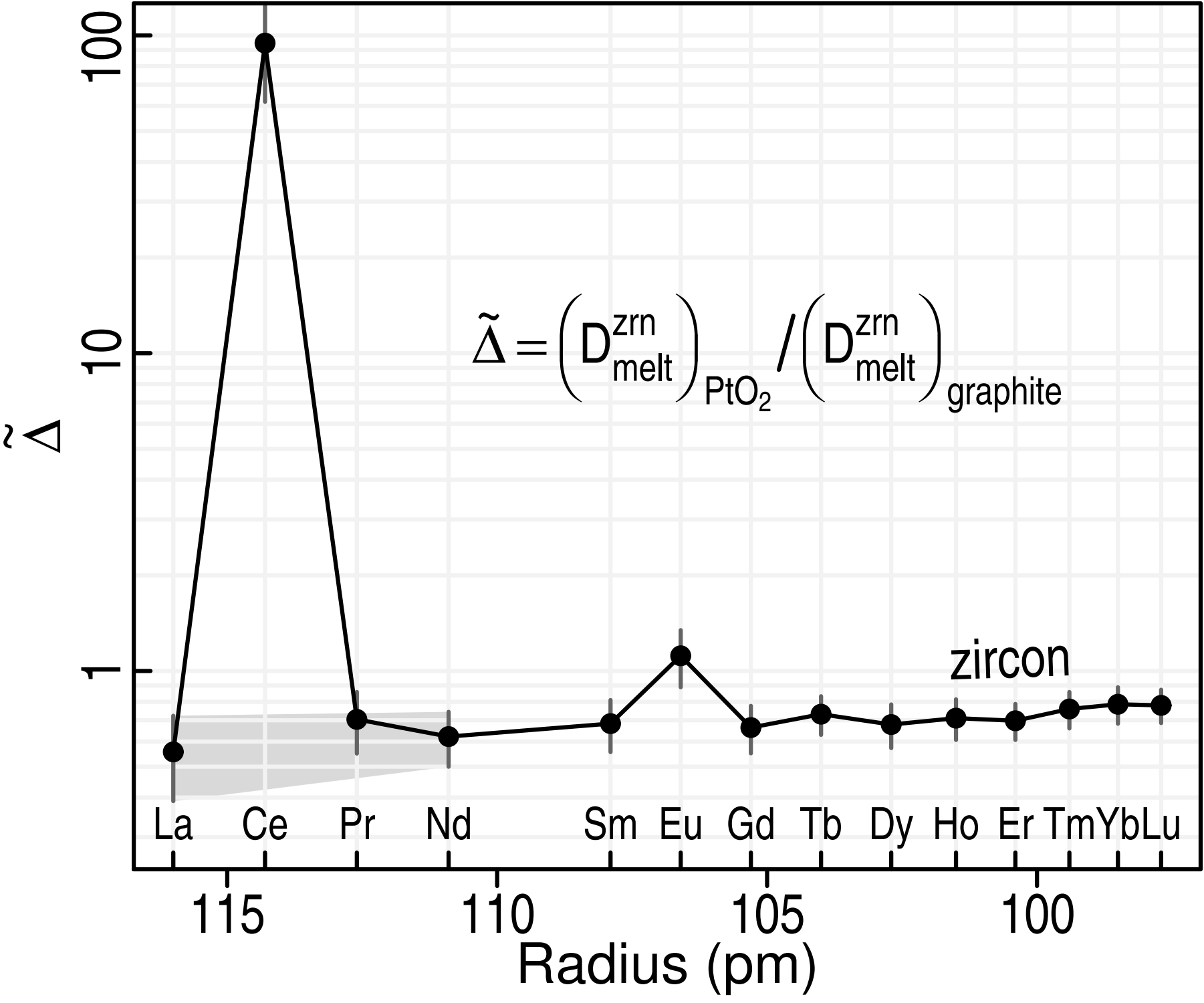
100
10
1
$\tilde{\Delta}$
$\tilde{\Delta} = \left(D^{zrn}_{melt}\right)_{PtO_2} / \left(D^{zrn}_{melt}\right)_{graphite}$
zircon
La
Ce
Pr
Nd
Sm
Eu
Gd
Tb
Dy
Ho
Er
Tm
Yb
Lu
115
110
105
100
Radius (pm)

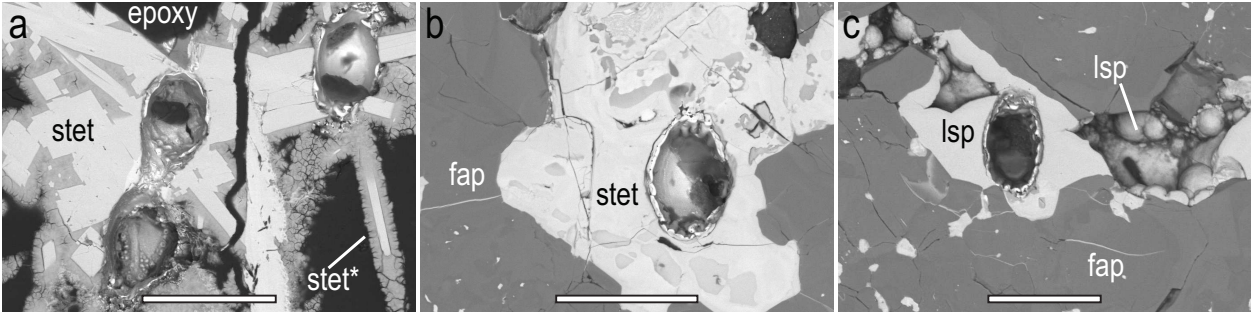
a
epoxy
stet
stet*
b
fap
stet
c
lsp
lsp
fap

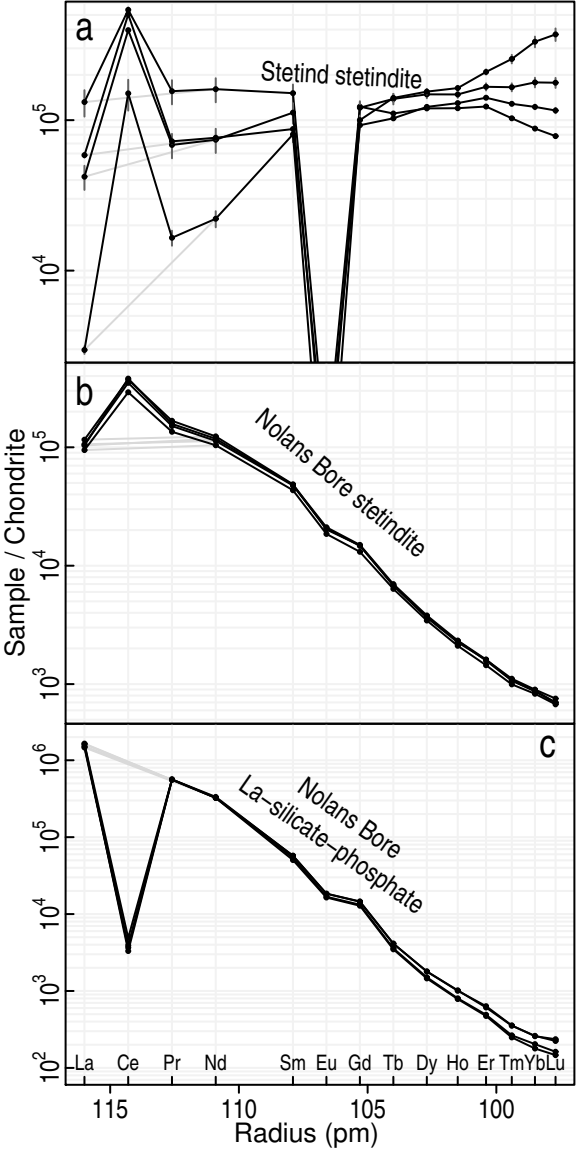
a
Stetind stetindite
b
Nolans Bore stetindite
c
Nolans Bore
La–silicate–phosphate
Sample / Chondrite
Radius (pm)
La Ce Pr Nd Sm Eu Gd Tb Dy Ho Er Tm Yb Lu
115
110
105
100

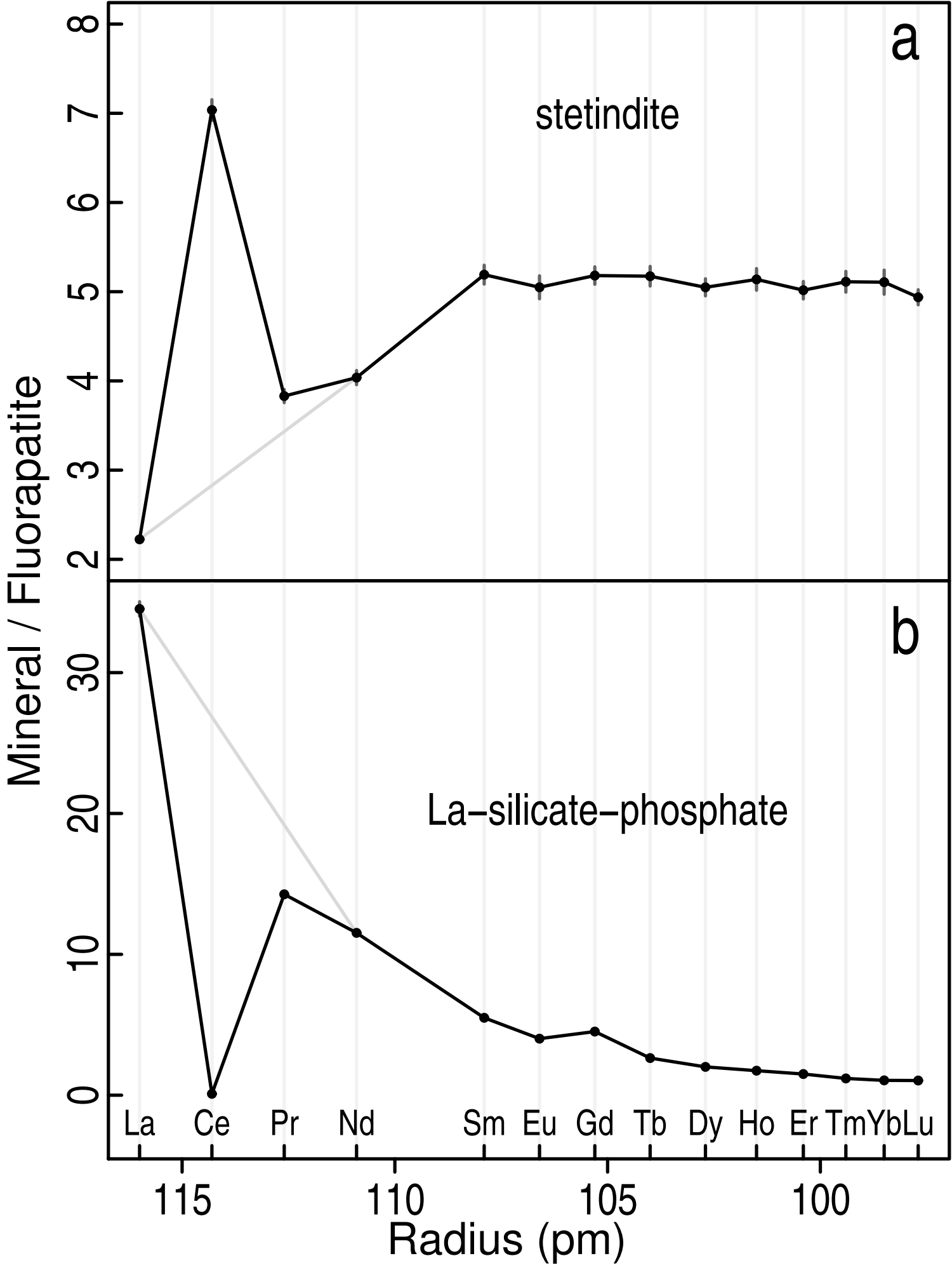
a
stetindite
b
La–silicate–phosphate
Mineral / Fluorapatite
2
3
4
5
6
7
8
0
10
20
30
La
Ce
Pr
Nd
Sm
Eu
Gd
Tb
Dy
Ho
Er
Tm
Yb
Lu
115
110
105
100
Radius (pm)

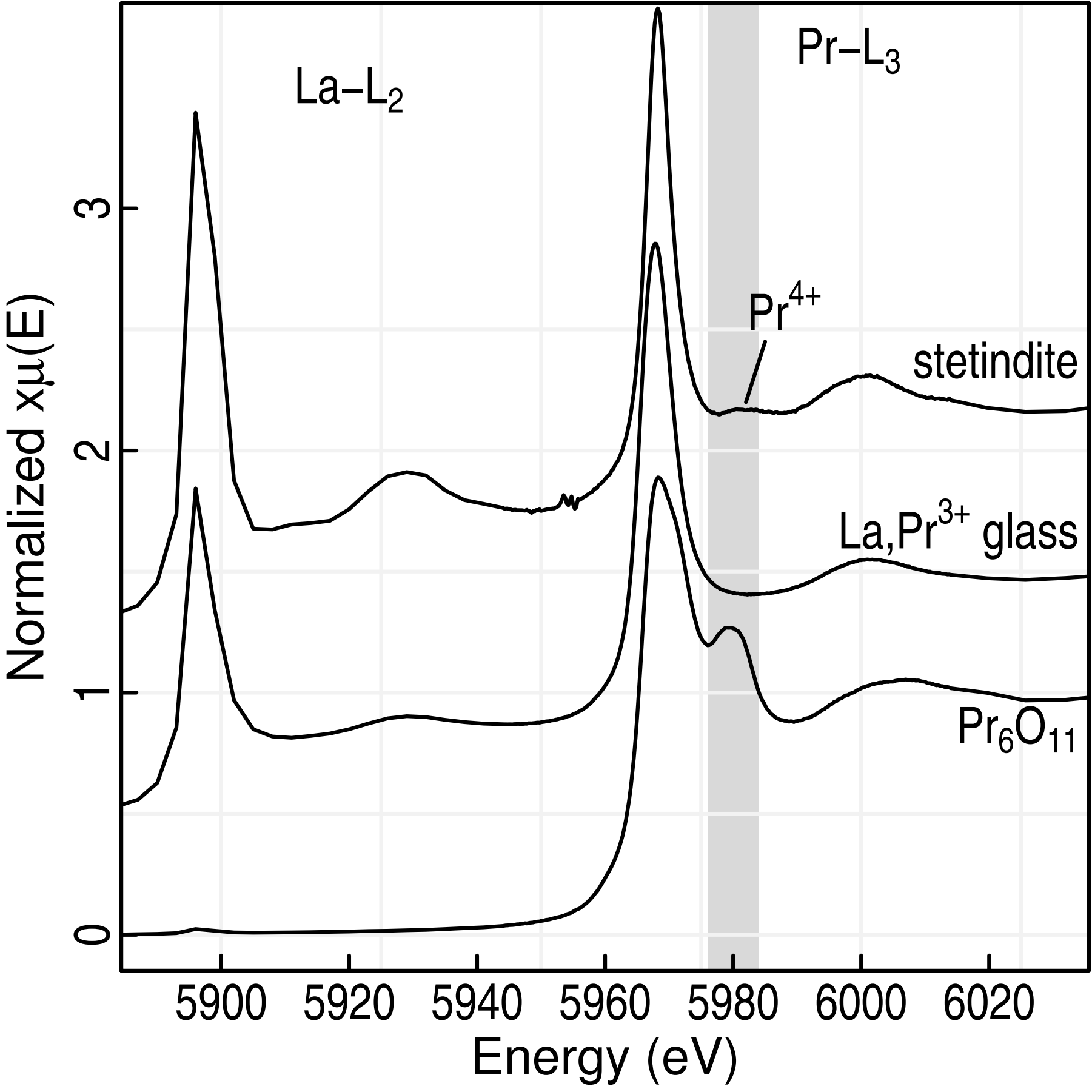
La–L2
Pr–L3
Pr4+
stetindite
La,Pr3+ glass
Pr6O11
Normalized xμ(E)
0
1
2
3
5900
5920
5940
5960
5980
6000
6020
Energy (eV)

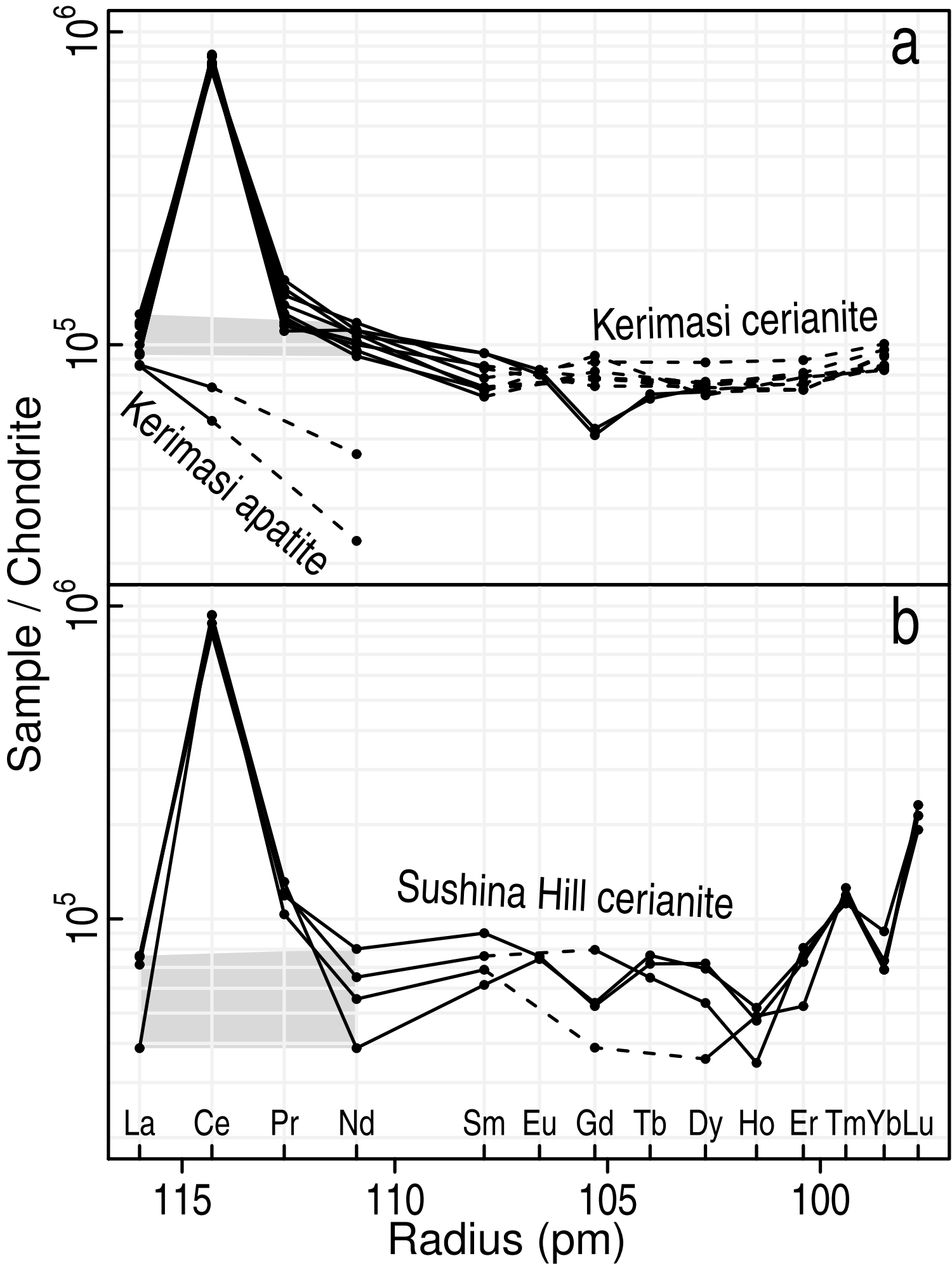
a
b
Kerimasi cerianite
Kerimasi apatite
Sushina Hill cerianite
Sample / Chondrite
10^6
10^5
La Ce Pr Nd Sm Eu Gd Tb Dy Ho Er Tm Yb Lu
115 110 105 100
Radius (pm)

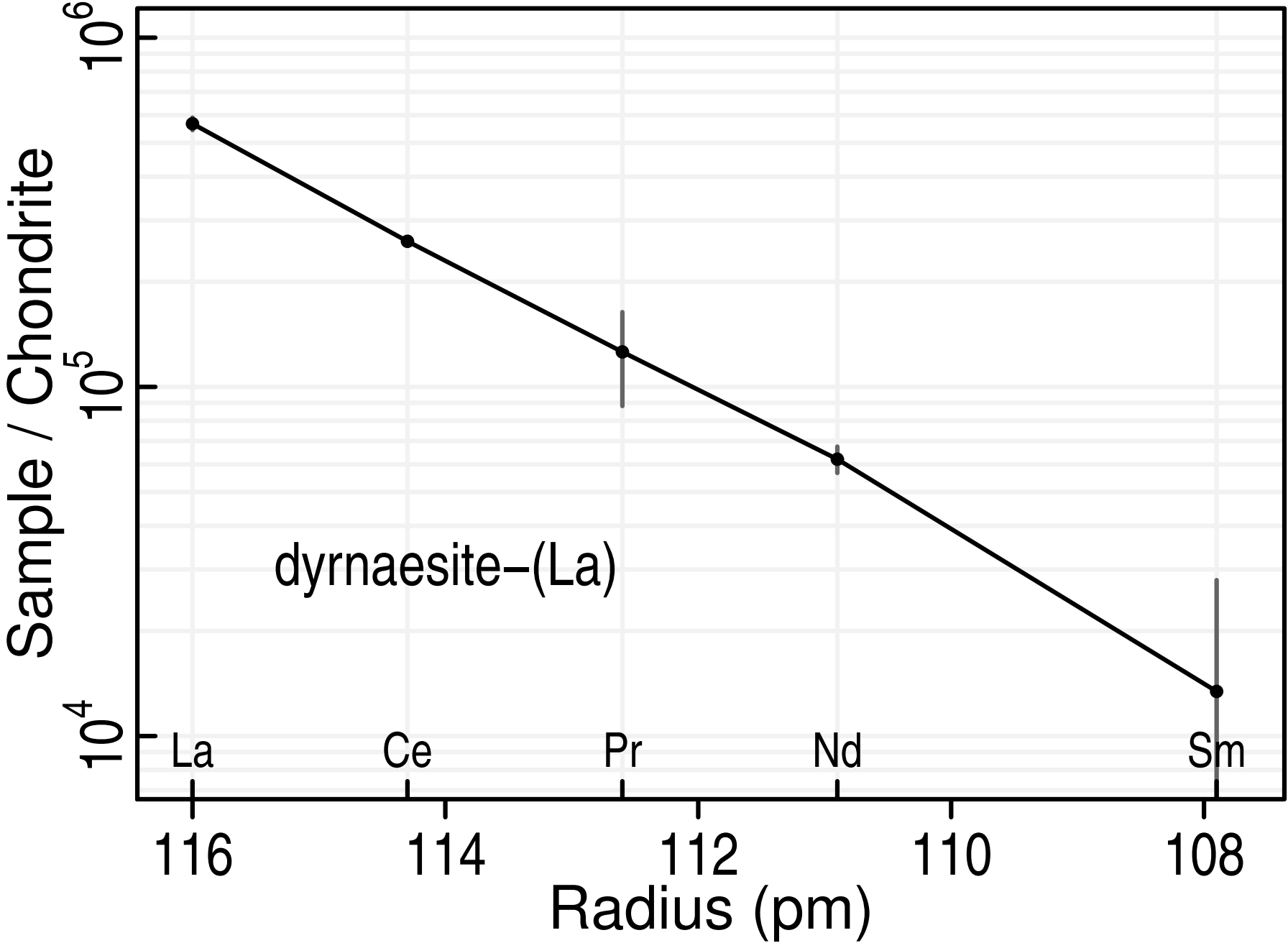
Sample / Chondrite
10^6
10^5
10^4
dyrnaesite–(La)
La
Ce
Pr
Nd
Sm
116
114
112
110
108
Radius (pm)